ECS Transactions, 23 (1) 389-396 (2009)
10.1149/1.3183743 © The Electrochemical Society

Impact of Confinement and Stress on the Subband Parameters in Ultra-Thin Silicon Films

V. Sverdlov[a], O. Baumgartner[a], T. Windbacher[a], F. Schanovsky[b], and S. Selberherr[a]

[a] Institute for Microelectronics
[b] Christian Doppler Laboratory for TCAD at the Institute for Microelectronics
TU Wien, Gußhausstraße 27-29, A-1040 Wien, Austria

The subband structure in thin silicon films under stress is rigorously analyzed. Calculations of the effective masses in the subbands show a dependence on shear strain and film thickness simultaneously. Both, the effective masses and the subband splitting determine the transport properties in silicon films. A decrease of the transport effective mass controlled by the shear strain component leads to a mobility enhancement even in ultra-thin silicon films. This increase of mobility and thus drive current combined with the improved channel control makes multi-gate MOSFETs based on thin films preeminent candidates for the 22nm technology node and beyond.

Introduction

Downscaling of MOSFETs as institutionalized by Moore's law is successfully continuing because of innovative changes in the technological processes and the introduction of new materials. The thereby made possible aggressive size reduction of semiconductor devices has lead to an enormous increase in computational power and speed of integrated circuits. The 32nm MOSFET process technology recently developed by Intel [1] involves new hafnium-based high-k dielectric/metal gates and represents a major change in the technological process since the invention of MOSFETs. Although alternative channel materials with a mobility higher than in silicon were already investigated [2, 3], it is commonly believed that strained silicon will be the main channel material even for MOSFETs beyond the 32nm technology node.

With scaling apparently approaching its fundamental limits, the semiconductor industry is facing critical challenges. New engineering solutions and innovative techniques are required to improve CMOS device performance. Strain-induced mobility enhancement is the most attractive solution to increase the device speed and will certainly take a key position among other technological changes for the next technology generations. In addition, new device architectures based on multi-gate structures with better electrostatic channel control and reduced short channel effects will be developed. A multi-gate MOSFET architecture is expected to be introduced for the 22nm technology node. Combined with a high-k dielectric/metal gate technology and strain engineering, a multi-gate MOSFET appears to be the ultimate device for high-speed operation with excellent channel control, reduced leakage currents, and low power budget.

Confining carriers within thin films reduces the channel dimension in transversal direction, which further improves gate channel control. The quantization energy in ultra-thin silicon films may reach a hundred meV. The parabolic band approximation usually employed for subband structure calculations of confined electrons inversion

layers becomes insufficient in ultra-thin silicon films. A recent study of subband energies and transport in (001) and (110) oriented films reveals that even non-parabolic isotropic dispersion is not sufficient to describe experimental data, and a direction-dependent anisotropic non-parabolicity must be introduced [4].

A comprehensive analysis of transport in multi-gate MOSFETs under general stress conditions is required for understanding the enhancement of device performance. Besides the biaxial stress obtained in silicon films grown epitaxially on a SiGe substrate, modern techniques allow the generation of large uniaxial stress along the [110] channel. Stress in this direction induces significant shear lattice distortion. The influence of the shear distortion on subband structure and low-field mobility has not yet been carefully analyzed.

The two-band **k·p** model [5-8] provides a general approach to compute the subband structure, in particular the dependence of the electron effective masses on shear strain. In case of a square potential well with infinite walls, which is a good approximation for the confining potential in ultra-thin silicon films, the subband structure can be obtained analytically [9]. This allows an analysis of subband energies, effective masses, non-parabolicity and the low-field mobility on film thickness for arbitrary stress conditions.

In the following we briefly review the main ideas behind the two-band **k·p** model for a valley in the conduction band of silicon. Then we shortly analyze the unprimed subband structure in (001) ultra-thin films, obtaining analytical expressions for the effective masses and non-parabolicity parameter. With these parameters the non-parabolic subband approximations for the subband dispersions are constructed. The non-parabolic subband dispersions are embedded into a subband Monte Carlo code in order to enable the computation of the low-field mobility. Results of the mobility enhancement calculations are finally analyzed.

Two-Band Hamiltonian

The subband structure in a confined system must be based on accurate bulk bands including strain, where several options are available. The conduction band dispersions computed with several methods in [100] and [110] directions are compared in Fig.1. The method based on non-local empirical pseudo-potentials from [10] is the most accurate one as compared to DFT band structure results obtained with VASP [11]. The $sp^3d^5s^*$ tight-binding model with parameters from [12] does not reproduce the anisotropy of the conduction band correctly. In addition, an accurate calibration of the parameters of the $sp^3d^5s^*$ model to describe the modification of the conduction band in strained silicon is still lacking.

The **k·p** theory is a well established method to describe the band structure analytically. As illustrated in Fig.1, the **k·p** method reproduces the band structure accurately at energies below 0.5eV, which is enough to describe the subband structure and transport properties of advanced MOSFETs. From symmetry consideration the two-band **k·p** Hamiltonian of a [001] valley in the vicinity of the *X* point of the Brillouin zone in silicon must be in the form [6]:

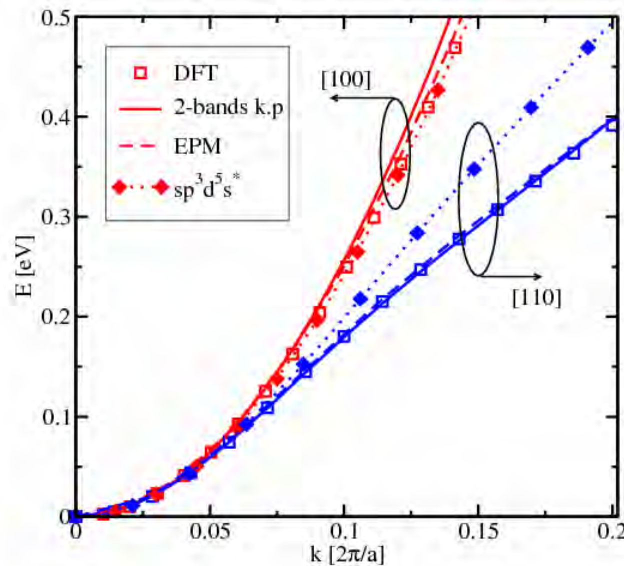

Figure 1. Comparison of bulk dispersions close at the minimum of the [001] valleys of the conduction band in [100] and [110] directions. DFT [11] and EPM [7,10] results are similar, while the sp^3d^5s* tight-binding model [12] underestimates anisotropy significantly.

$$H = \left(\frac{\hbar^2 k_z^2}{2m_l} + \frac{\hbar^2 (k_x^2 + k_y^2)}{2m_t} \right) I + \left(D\varepsilon_{xy} - \frac{\hbar^2 k_x k_y}{M} \right) \sigma_z + \frac{\hbar^2 k_z k_0}{m_l} \sigma_y \tag{1}$$

$\sigma_{y,z}$ are the Pauli matrices, I is the 2×2 unity matrix, m_t and m_l are the transversal and the longitudinal effective masses, $k_0 = 0.15 \times 2\pi / a$ is the position of the valley minimum relative to the X point in unstrained silicon, ε_{xy} denotes the shear strain component, $M^{-1} \approx m_t^{-1} - m_0^{-1}$, and D=14eV is the shear strain deformation potential [5-8]. The two-band Hamiltonian results in the following dispersion relations [6]:

$$E = \frac{\hbar^2 k_z^2}{2m_l} + \frac{\hbar^2 (k_x^2 + k_y^2)}{2m_t} \pm \sqrt{\left(\frac{\hbar^2 k_z k_0}{m_l} \right)^2 + \delta^2} \tag{2}$$

The negative sign corresponds to the lowest conduction band,

$$\delta^2 = (D\varepsilon_{xy} - \hbar^2 k_x k_y / M)^2 . \tag{3}$$

All moments as well as energies in (2) are counted from the X-point of the Brillouin zone. The classical parabolic approximation is obtained from (2), when coupling between the two conduction bands described by the parameter δ is neglected. Coupling between the bands is small, when the wave vectors $|k_x|$, $|k_y| << k_0 (M/m_l)^{1/2}$ and shear strain ε_{xy} = 0. Due to band coupling the dispersion relations (2) become non-parabolic in strained silicon, if the shear strain component is non-zero, and/or at higher energies. In order to check the accuracy of (2) we have carried out numerical band

structure calculations with the empirical pseudo-potential method (EPM) with parameters from [7,10]. Excellent agreement between the two-band **k·p** model (1) and the EPM results was found up to an energy of 0.5eV. Equation (2) is valid in a larger range of energies compared to a parabolic dispersion relation with isotropic non-parabolic correction and can be used to determine the subband structure in thin films.

Subbands in Ultra-Thin Silicon Films

For [001] silicon films the confinement potential gives an additional contribution $U(z)I$ to the Hamiltonian (1). In the effective mass approximation described by (1) with the coefficient in front of σ_x set to zero, the confining potential $U(z)$ is known to quantize the six equivalent valleys of the conduction band of bulk silicon into the four-fold degenerate primed and the two-fold degenerate unprimed subband ladder [12]. In ultra-thin films the unprimed ladder is predominantly occupied. In order to analyze the subbands, we approximate the confining potential of an ultra-thin silicon film by a square well potential with infinite potential walls. Generalization to include a self-consistent potential is straightforward though numerically involved [13].
Because of the two-band Hamiltonian, the wave function Ψ is a spinor with the two components |0> and |1>. For a wave function with space dependence in the form $\exp(ik_z z)$ the coefficients A_0 and A_1 of the spinor components are related via the equation $H\Psi = E(k_z)\Psi$. For a particular energy E there exist four solutions k_i (i=1,…,4) for k_z of the dispersion relation (2), so the spatial dependence of a spinor component is in the form $\sum_{i=1}^{4} A_\alpha^i \exp(ik_i z)$. The four coefficients are determined by the boundary conditions that both spinor components are zero at the two film interfaces. This leads to the following dispersion equations:

$$\tan\left(k_1 \frac{k_0 t}{2}\right) = \frac{k_2}{\sqrt{k_2^2+\eta^2} \pm \eta} \frac{\sqrt{k_1^2+\eta^2} \pm \eta}{k_1} \tan\left(k_2 \frac{k_0 t}{2}\right) \tag{4}$$

$\eta = m_l\,|\delta|/(\hbar k_0)^2$. If the value of

$$k_2 = \sqrt{k_1^2 + 4 - 4\sqrt{k_1^2+\eta^2}} \tag{5}$$

becomes imaginary at high η values, the trigonometric functions in (4) are replaced by the hyperbolic ones. Special care must be taken to choose a correct branch of $\sqrt{k_2^2+\eta^2}$ in (5): the sign of $\sqrt{k_2^2+\eta^2}$ must be alternated after the argument becomes zero. Introducing $y_n = (k_1 - k_2)/2$, (4) can be written in the form [14]:

$$\sin(y_n k_0 t) = \pm \frac{\eta y_n \sin\left(\frac{1-\eta^2-y_n^2}{1-y_n^2} k_0 t\right)}{\sqrt{(1-y_n^2)(1-\eta^2-y_n^2)}} \tag{6}$$

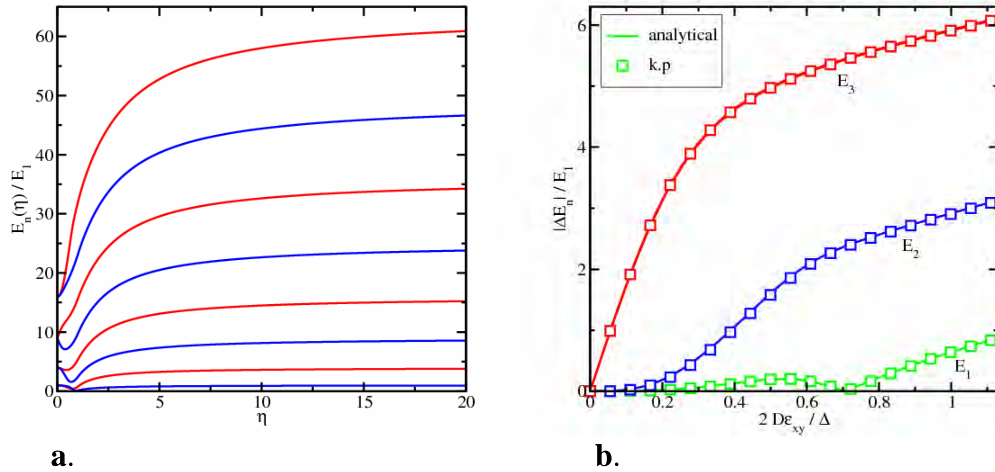

a. **b.**

Figure 2 **a**. Normalized positions of the subband minima with respect to the strain-dependent conduction band minimum as function of dimensionless shear strain for a film of the thickness *t*=5.43nm.
b. Strain-dependent splitting between the minima of the unprimed subbands with the same *n*.

We solve (6) by perturbation techniques. For small η and thick films the right-hand side in (6) can be ignored. The subband relations are found from the condition

$$y_n = \pi n/(k_0 t)\,. \tag{7}$$

Substituting (7) into the right-hand side of (6) and solving (6) for small strain η one obtains the following dispersion relation for the unprimed subbands *n*:

$$E_n^{\pm} = \frac{\hbar^2}{2m_l}\left(\frac{\pi n}{t}\right)^2 + \hbar^2 \frac{k_x^2 + k_y^2}{2m_t} \pm \left(\frac{\pi n}{k_0 t}\right)^2 \frac{\left| D\varepsilon_{xy} - \frac{\hbar^2 k_x k_y}{M} \right|}{k_0 t \left| 1 - (\pi n / k_0 t)^2 \right|} \sin(k_0 t) \tag{8}$$

It follows that the subband degeneracy is preserved only, when shear strain is zero and either k_x=0 or k_y=0. (8) demonstrates that the unprimed subbands are *not equivalent*. We first analyze the splitting in energy between the two unprimed subbands with the same *n*, which is usually called the valley splitting [12]. According to (8), shear strain induces a valley splitting linear in strain, for small shear strain values [14]:

$$\Delta E_n = 2\left(\frac{\pi n}{k_0 t}\right)^2 \frac{D\varepsilon_{xy}}{k_0 t \left| 1 - (\pi n / k_0 t)^2 \right|} \sin(k_o t) \tag{9}$$

The valley splitting is inversely proportional to $(k_0 t)^3$ and oscillates with the film thickness, in agreement with earlier work [12,15].
To find the valley splitting at higher strain values, (6) must be solved numerically. Results shown in Fig.2 demonstrate that valley splitting can be effectively controlled by adjusting the shear strain and modifying the effective thickness *t* of the electron system. It is interesting to note that for extremely high strain values the dispersion of the lowest

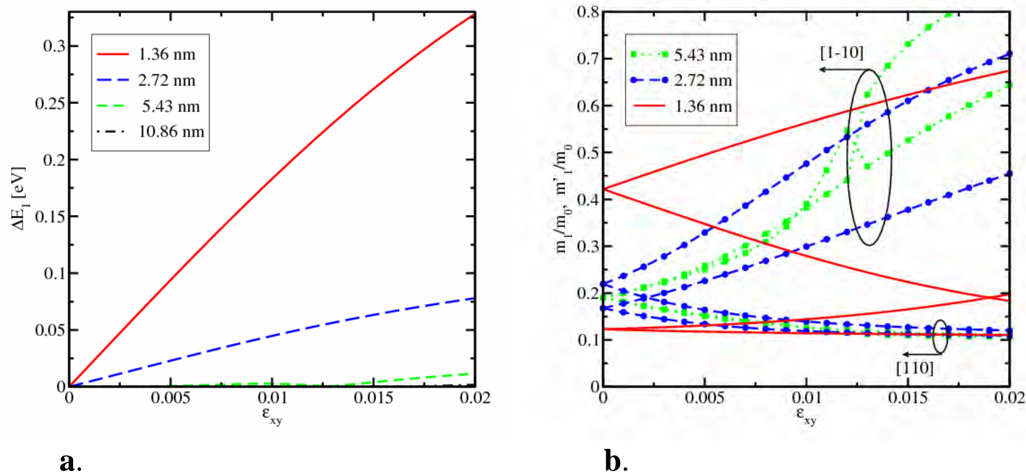

a. **b.**

Figure 3 **a**. Shear strain induced splitting of the ground subbands for several film thicknesses. In ultra-thin films splitting is larger than kT already for moderate stress. **b**. Effective masses of the two ground subbands. In ultra-thin films effective masses of the two ground subbands are different even without stress.

conduction band becomes parabolic again, and the quantization levels in a square well potential are therefore recovered in this limit. Although the value of strain in this limit is unrealistic, this result will be used to analyze dispersion relations for the primed subbands.

Uniaxial stress along [110] channel direction, which induces shear strain, is already used by industry to enhance the performance of modern MOSFETs. Therefore, its application to control valley splitting does not require expensive technological modifications. A possibility to introduce valley splitting larger than the Zeeman spin splitting makes silicon promising for future spintronic applications [16].

As seen from Fig.3a, the valley splitting in ultra-thin silicon films can be quite large already for reasonable stress values. In this case the higher subband becomes depopulated, prompting for mobility enhancement in (001) ultra-thin films strained along [110] direction.

The dispersion relation (9) predicts different effective masses in [110] direction for the unprimed subbands with the same n even without strain:

$$m_{(1,2)} = \left(\frac{1}{m_t} \pm \frac{1}{M} \left(\frac{\pi n}{k_0 t} \right)^2 \frac{\sin(k_o t)}{k_0 t \left| 1 - (\pi n / k_0 t)^2 \right|} \right)^{-1} \tag{10}$$

Numerically found values of the masses for the two ground subbands are shown in Fig.3b. Contour plots of the subband dispersions for the two ground subbands are shown in Fig.4. It is to note, that the subband dispersions are not equivalent. This has a profound effect on the valley splitting. Without shear strain the Landau levels in the external [001] magnetic field B are determined using the Bohr-Sommerfeld quantization conditions:

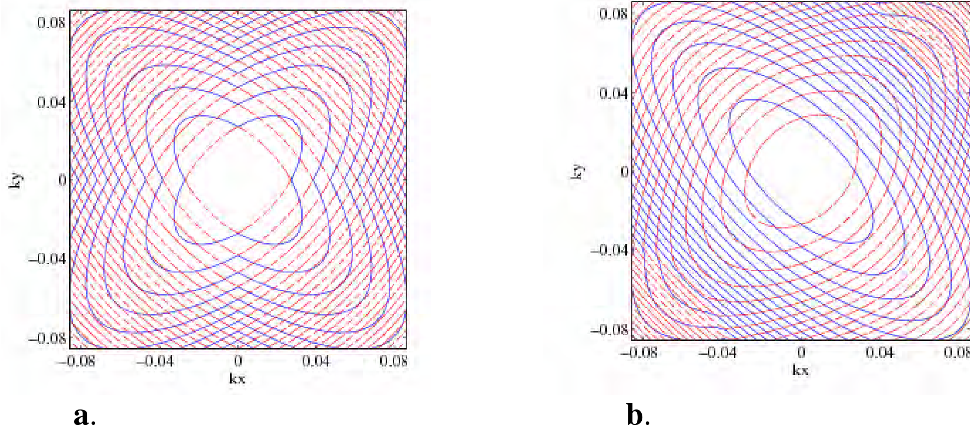

Figure 4 Dispersions of the two ground subbands for a film thickness of 1.36nm:
a. Without strain the subbands are degenerate at the minimum. The lower subband dispersion is described by the unification of the two ellipses with different masses (10), while the second subband is described by their intersection. The difference in quasi-classical orbits of the motion in the magnetic field is responsible for the subband splitting (11) in orthogonal magnetic field.
b. Shear strain of 1% removes the degeneracy between the minima of the ground subbands shown in Fig.3a. The subband dispersions are now characterized by the corresponding effective masses in [110] and [1-10] directions (Fig.3b).

$$E_m^{(1,2)} = \hbar\omega_c\left(m+\frac{1}{2}\right)\frac{\pi}{4\arctan\left(\sqrt{m_{(1,2)}/m_{(2,1)}}\right)}, \tag{11}$$

where $\omega_c = \frac{eB}{\sqrt{m_1 m_2}c}$ is the cyclotron frequency. Therefore, the magnetic field induces a valley splitting linear in the field strength B, in agreement with recent experimental results [16].

A large value of the valley splitting observed by measuring conductance through a point contact can also be attributed to the difference in the subband dispersions, in particular, to the effective mass difference (10). Indeed, confining the electron system laterally in [1-10] direction by the potential, the following dispersion relation of propagating modes within the point contact is obtained:

$$E_p^{(1,2)} = \frac{k^2 k_x'^2}{2m_{(2,1)}} + \hbar\omega_{(1,2)}\left(p+\frac{1}{2}\right)+V_b \tag{12}$$

Here $\omega_{(1,2)}^2 = \kappa / m_{(1,2)}$ and V_b is a gate voltage dependent shift of the conduction band in the point contact [17]. The energy minima of the two propagating modes with the same p are separated by $\Delta E_p = \hbar\,|\,\omega_1 - \omega_2\,|$ and they are resolved in the conductance of a point contact as two distinct steps. The difference in the effective masses (10) and,

correspondingly, the valley splitting can be greatly enhanced by reducing the effective thickness *t* of the film.

Conclusion

A rigorous analysis of the subband structure in thin silicon films is performed. The thickness dependence of the effective mass of primed subbands calculated within the two-band **k·p** model is in agreement with the earlier full-band calculations. It is demonstrated that within the two-band **k·p** model the unprimed subbands with the same quantum number *n* are not equivalent. A large splitting between the unprimed valleys of ultra-thin films can be introduced by a shear strain component. Calculated subband effective masses are shown to depend on shear strain and thickness simultaneously. Interestingly, the effective masses of the two unprimed valleys are different in ultra-thin silicon films even without strain. This results in a linear dependence of the subband splitting on the magnetic field strength and leads to large subband splitting in a laterally confined electron system in a point contact.

Acknowledgments

This work was supported in part by the Austrian Science Fund FWF, project P19997-N14, and by funds from FWF, project I79-N16, CNR, EPSRC and the EC Sixth Framework Programme, under Contract N. ERAS-CT-2003-980409 as part of the European Science Foundation EUROCORES Programme FoNE.

References

1. S.Natarajan, M.Armstrong, H.Bost, *et al.*, *IEDM 2008*, pp.941-943.
2. M.K.Hudati, G.Dewey, S.Datta, *et al.*, *IEDM 2007*, pp.625-628.
3. R.Chau, *ISDRS 2007,* p.3.
4. K.Uchida, A.Kinoshita, and M.Saitoh, *IEDM 2006*, pp.1019-1021.
5. J.C.Hensel, H.Hasegawa, and M.Nakayama, *Phys.Rev. 138*, A225-A238 (1965).
6. G.L.Bir and G.E.Pikus, Symmetry and Strain-Induced Effects in Semiconductors, J.Willey & Sons, NY, 1974.
7. E.Ungersboeck, S.Dhar, G.Karlowatz, *et al.*, *IEEE T-ED* 54, 2183-2190 (2007).
8. V.Sverdlov, E.Ungersboeck, H.Kosina, *et al.*, *ESSDERC 2007*, pp.386-9.
9. V.Sverdlov, G.Karlowatz, S.Dhar, *et al.*, *Sol.State Electron*. 52, 1563-1568 (2008).
10. M.Rieger and P.Vogl, *Phys.Rev. B* 48, 14275-14287 (1993).
11. VASP (Vienna Ab-initio Simulation Program) G.Kresse and J. Hafner, *Phys.Rev. B* 47, 558 (1993); ibid. *B* 49, 14251 (1994); G.Kresse and J. Furthmueller, *Phys.Rev. B* 54, 11169 (1996); *Comput.Mat.Sci*. 6, 15 (1996).
12. T.Ando, A.B.Fowler, and F.Stern, *Rev.Mod.Phys*. 54, 437-672 (1982).
13. O.Baumgartner, M.Karner, V.Sverdlov, *et al.*, *EUROSOI 2009*, pp.57-58.
14. V.Sverdlov and S.Selberherr, *Sol.State Electron*. 52, 1861-1866 (2008).
15. M.Friessen, S.Chutia, C.Tahan, *et al., Phys.Rev.B* 75, 115318-1—12 (2007).
16. S.Goswami, K.A.Slinker, M.Friesen, *et al., Nature Physics* 3, 41-45 (2007).
17. B.J.van Wees, H.van Houten and C.Beenakker, *Phys.Rev.Lett*., 60, 848-850 (1988).